near-infrared range (NIR: 600-2,500 nm) [25]. This imaging modality shows attractive data from organs close to skin in small animals, but this is likely to remain restricted to relatively superficial targets because of the absorbing and scattering properties of tissue in the visible range and NIR [26].

3.1 *Fluorescence Imaging*

Fluorescence is light of a visible color emitted from a substance under stimulation or excitation by light or other forms of electromagnetic radiation. The light is given off only while the stimulation continues. Visible light is used to excite fluorescence within the subject, and a camera or fluorescence microscopy system detects the emitted light from the region of interest. The commonly used strategy is to fluorescently tag the cells, tissue, or molecules under investigation with substances known to fluoresce. The most popular fluorochrome is green fluorescent protein (GFP), which is derived from the jellyfish *Aequorea victoria*. The wild-type GFP emits light at 509 nm, whereas its variant EGFP has a longer emitting wavelength and is 35-fold brighter [24]. Thus there are a lot of fluorescent proteins, and increasing numbers of new bright fluorescent probes with a variety range of emission wavelengths and greater stability have been developed and are now available [46].

Fluorochromes of wavelengths greater than 600 nm should be used in order to minimize absorbance by surrounding tissue and to distinguish background and autofluorescence [49]. Indeed, the use of NIR fluorochromes achieves maximum tissue penetration and minimum background and autofluorescence [53], and several applications have exploited the NIR range [29] with best results typically achieved when the emission wavelengths of the dye are between 500 and 950 nm [30].

3.2 *Bioluminescence Imaging*

Bioluminescence is biochemical emission of light, with very little heat, by living organisms such as fireflies and deep-sea fishes as the result of a chemical reaction during which chemical energy is converted to light energy. This reaction is mediated by one of the luciferase family of photoproteins that can be isolated either from the sea pansy (*Renilla reniformis*) or from the North American firefly (*Photimus pyralis*). Different organisms produce different bioluminescent substances and use different substrates. Marine bioluminescent organisms use coelenterazine as a substrate, and terrestrial organisms use d-luciferin, which provides a longer-lived and longer wavelength. Luciferase is normally bound to ATP (adenosine triphosphate) in an inactive form, but in catalysis of luciferin it is liberated from the ATP and combines with oxygen to form an oxyluciferin in an excited state, which quickly decays, emitting photons of visible light as it does [54].

As in the case of fluorescence imaging (FLI), the use of luciferases that have a significant portion of their emission greater than 600 nm, such as luciferase derived from fireflies and click beetles (approximately 60% of the light emitted from these two enzymes has wavelengths greater than 600 nm), will lead to more sensitive detection of the labeled cells in vivo [38, 55].

In vivo bioluminescence imaging (BLI) has been applied in the assessment of the extent of tumor growth and response to therapy by transplantation of tumor cells transfected to express luciferase into animals [47]. Furthermore, the expression of luciferase can be controlled so that it is only expressed when a gene of interest is being transcribed [5, 31]. Cells expressing luciferase in animal models can be easily identified through their emission of light in the range of 400-620 nm by administration of luciferin [19]. This technology has become an invaluable tool that has been employed to dynamically monitor tumor growth or transcriptional activity in living animals.

3.3 *Comparison of* BLI *with* FLI

First of all, as the luciferase reaction is energy-dependent and requires ATP and oxygen, the luminescent signal is produced only from living cells, which are different from the fluorescent signals that can be sustained even in nonliving cells. The major attraction of BLI over FLI is that, although absolute light levels generated by the targets may be low, photons are generated generally only where luciferase is present, leading to an extremely low level of background signals and excellent signal-to-noise ratios (SNRs). In contrast, FLI requires an external light source to stimulate the emission of light from the probe, and the light source could also generate bright background signals arising from the animal's intrinsic autofluorescence [26, 44, 50].

However, there are some limitations in BLI. First, light transmission efficiency is dependent on the type and location of tissue being assessed because of the narrow range, from 400 nm to 620 nm, of the light emission peak. Highly vascular organ structures contain hemoglobin that absorbs transmitted light, which results in about a ten-fold reduction of the bioluminescent signal for every centimeter of tissue depth [10]. Second, because the catalytic reaction in BLI is time- and enzyme-dependent, the window period for optimum image capture must be determined [25].

In contrast, a distinctive advantage of FLI over BLI is that it does not require administration of a substrate for visualization. FLI may be more convenient and allow easier capture of images at multiple time points, since administration of a substrate into the animal is not required. In addition, FLI is a more flexible technology, since it permits the use of a far wider range of probes, labeling methods, and targets. The number of photons emitted in FLI is orders of magnitude greater than that in BLI [26, 50].

Among the great number of fluorescent probes, Quantum Dots (Q-Dots), which are semiconductor nanocrystals that have long-term stability and fluoresce brightly up to the NIR spectrum on excitation, have been developed for imaging [1]. Q-dots enable antibody-targeted spectral imaging and analysis such as examining the

distribution of Q-dot-labeled antitumor antibodies in mice [14]. In addition, this method will be available as multimodal contrast agents for not only FLI but also PET or MRI detection [33]. An agent such as Q-Dots is valuable in multimodality imaging as described below.

4 Multimodality Imaging

Imaging modalities can be divided into two groups. One group includes ultrasound, CT, and MRI, providing structural information, while another group includes SPECT, PET, and optical imaging, providing functional or molecular information. Both groups have some drawbacks and advantages (Tables 1 and 2). Therefore, the combination of different imaging modalities has been developed to offset the disadvantage of each modality, and it will develop into a powerful tool with the recent development of contrast agents including Q-Dots as mentioned in the previous section.

PET/CT has only recently developed to enable accurate diagnosis. By combining the structural anatomic information of CT scans with the metabolic or cellular activity data of PET scans, it has become possible to visualize anatomy and function simultaneously. The anatomic information enables compensation of the correlated radionuclide data for physical perturbations such as photon attenuation, scatter radiation, and partial volume errors. Thus, dual-modality imaging provides a priori information that can improve both the visual quality and the quantitative accuracy of the radionuclide images. The hybrid imaging of PET/CT has been shown to improve not only the sensitivity of PET interpretation but also its specificity. Micro-PET/CT is used for small animals to obtain high anatomic resolution with functional information [48, 49]. The combination of the various modalities, called multimodality imaging, offers valuable information. By the same token, SPECT/CT [18] and optical PET [43] have been developed in addition to PET/CT.

A further development in FLI is fluorescence molecular tomography (FMT), which has been developed for acquiring images of fluorescently labeled proteins and for deeper targets. It employs continuous wave or pulsed light from different sources to excite the fluorochrome label, and multiple detectors are arranged spatially around the subject analogous to the set-up in CT or MR scanners [39, 40]. Computation of the data generates a 3D image. The resulting images have a resolution of 1-2 mm, and the fluorochrome detection threshold is in the nanomolar range [25].

5 A Novel In Vivo Imaging System of the Endometrial Model Mouse

As the bioluminescent signal is emitted only from living cells expressing luciferase, leading to low background noise, we chose BLI as the modality to visualize an artificial menstrual cycle in mice and developed an in vivo imaging system based on this concept.

Table 1 The properties of currently available in vivo imaging techniques

Modality	Basis	Reagents	Acquisition time	Tissue penetration depth	Spatial resolution	Signal quantification capabilities	Cost (equipment and usage)
Ultrasound	High-frequency sound waves	Microbubbles	minutes	1–200 mm	50–500 μm (animal) 0.1–1 mm (clinical)	Low	Low
CT	X-rays	Iodine	minutes	No limit	30–50 μm (animal) 0.5–1 mm (clinical)	N/A	Medium-high
MRI	Radio frequency waves	Paramagnetic cation probes	minutes–hours	No limit	25–100 μm (animal) 0.2 mm (clinical)	Medium	High
PET	High energy γ-rays	^{18}F, ^{11}C, ^{13}N, ^{15}O, ^{124}I, ^{94m}Tc labeled probes or substrates for reporter transgenes	minutes	No limit	1–2 mm (animal) 6–10 mm (clinical)	High	High
SPECT	Low energy γ-rays	^{99m}Tc, ^{111}In, ^{125}I labeled probes	minutes	No limit	1–2 mm (animal) 7–15 mm (clinical)	Medium-high	Medium-high
FLI	Visible to near-infrared light	Fluorescent proteins, fluorescent dyes, and quantum dots (semiconductor)	seconds–minutes	1–20 mm	1–10 mm (animal) (depending on tissue depth)	Low-medium	Low
BLI	Visible light	Luciferase and substrates (luciferin, coelenterazine)	seconds–minutes	1–10 mm	1–10 mm (animal) (depending on tissue depth)	Low-medium	Low

Table 2 Advantages and disadvantages of in vivo imaging modalities

Modality	Advantages	Disadvantages
Ultrasound	Real-time imaging, low cost, and user-friendly	Limited ability to image through bone or lungs
CT	Good anatomic resolution	Relatively poor soft-tissue contrast Radiation to animal with CT contrast agents
MRI	Highest spatial resolution The ability to combine functional information and anatomic details	Low sensitivity Long acquisition time Long image processing time
PET	High sensitivity The ability of quantitative measure Variety of probes and strategies confers a high degree of versatility	Low resolution Unincorporated substrate can increase noise Cyclotron required to generate short-lived radioisotope Radiation to animal
SPECT	Multiple probes can be detected simultaneously Radioisotopes have longer half-lives than those used in PET	10–100x less sensitive than PET Relative low resolution Radiation to animal
FLI	High sensitivity Easy and quick to image Multiple reporter wavelengths enables multiplex imaging Detect fluorochromes in live and dead cells Transgene-based approach confers versatility	Prone to attenuation with increased tissue depth Probes with emission wavelength <600 nm prone to autofluorescence of nonlabeled cells
BLI	High sensitivity Easy and quick to image Provides relative measure of cell viability or function Available for gene expression and cell tracking Transgene-based approach confers versatility	Low anatomic resolution Light emission prone to attenuation with increased tissue depth

5.1 Lentiviral Introduction of Reporter Genes into Primary Endometrial Cells

We have developed a recombinant lentivirus capable of introducing and stably expressing both the Venus [a yellow fluorescent protein (YFP) mutant] [35] gene and the click beetle red-emitting luciferase (CBR luc, a luciferase variant) [55] gene in the targeted cells (Fig. 1a). These two reporter markers are useful for

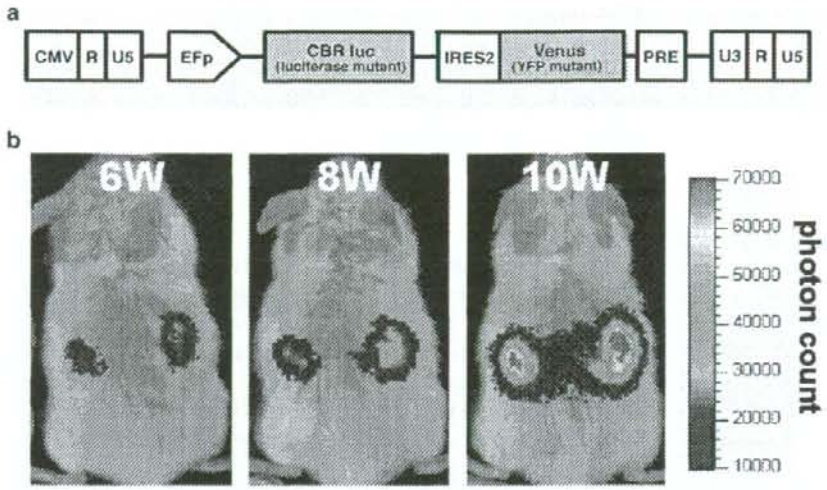

Fig. 1 Lentiviral construct for fluorescence and bioluminescence and optical bioluminescence images of the growth of the tissues reconstructed from lentivirally transduced SDECs in living NOG mice. **a** Lentiviral construct encoding a dual function CBR luc (a luciferase variant) and Venus (a YFP variant) bicistronic reporter gene connected via an internal ribosomal entry site (*IRES*). **b** Representative sequential BLI of NOG mice treated for different durations with two E_2 pellets

flow cytometry sorting and the detection of living cells from outside the body, respectively. Indeed, fluorescence microscopy-revealed Venus signals were detected in lentivirally-infected cells, and these cells could be sorted easily by flow cytometry. Moreover, CBR luc (maximum emission at 613 nm) has the potential to pass through thicker tissue. By combining the advantages of the lentivirus and CBR luc, we successfully assessed the dynamic state of the endometrial reconstructs in living NOD/SCID/γ_c^{null} (NOG) mice [23].

5.2 *Noninvasive, Real-Time, and Quantitative Assessment of the Reconstructs by BLI*

We transplanted singly dispersed endometrial cells (SDECs) beneath the kidney capsules of severely immunodeficient mice, NOG mice, and we demonstrated for the first time that a functional endometrium-like structure can be regenerated from SDECs [32]. This model is the humanized mouse we developed. To apply this humanized mouse to an in vivo BLI system, we transplanted the human endometrial cells infected with our above-mentioned lentivirus beneath the kidney capsule. Consequently, sequential BLI of the ventrally positioned estradiol (E_2)-treated NOG mouse 6-10 weeks after xenotransplantation revealed bioluminescent (CBR) signals in locations corresponding to the bilateral kidneys (Fig. 1b).

Furthermore, we showed that the signal intensities reflecting the volume of the reconstructed tissue were enhanced in an E_2 dose- and time-dependent manner by using ovariectomized NOG (OVX-NOG) mice without or with one or two long-term continuous release pellets of E_2 (Fig. 2a). This means that in our system the growth behavior of the reconstructed tissue could be assessed quantitatively and sequentially.

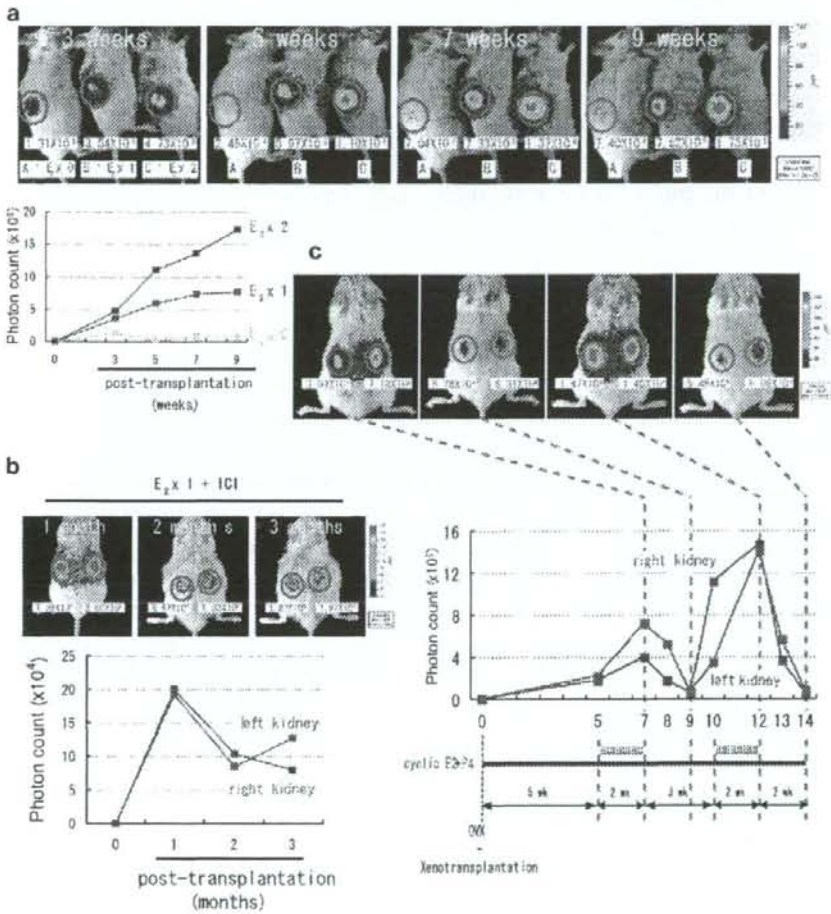

Fig. 2 Quantitative assessment of the growth of the regenerated endometrium. **a** Representative BLI (***top panels***) and serial photon count measurements (***bottom panel***) of NOG mice treated for different durations with the various indicated doses of E_2 pellets. The photon count value of each region of interest (ROI, *red circle*) is indicated. **b** Representative BLI (***top panels***) and serial photon count measurements (***bottom panel***) of a xenotransplanted OVX-NOG mouse treated with E_2 in combination with daily injections of ICI 182,780, a pure estrogen antagonist. **c** Representative sequential BLI (***top panels***) and serial photon count measurements (***middle panel***) of a xenotransplanted OVX-NOG mouse undergoing cyclic E_2+P_4 treatment (***bottom panel***) to induce artificial menstrual cycle-related changes. Images are adapted, with permission, from Ref. 53 Copyright 2007, National Academy of Sciences, USA

Additionally, in contrast to the xenotransplanted mice treated with E_2 alone, the signal intensity was not increased but rather decreased 2-3 months after cotreatment with E_2 in combination with ICI-182,780 (ICI), a pure estrogen antagonist [51] (Fig. 2b). These data indicated that the antagonistic effect of ICI can be noninvasively and successfully assessed and this system could be used as a tool for drug screening.

Finally, we monitored the dynamic changes of the endometrial reconstructs during an artificial menstrual cycle induced by cyclic treatment with E_2 in combination with P_4 ($E_2 + P_4$ treatment). Sequential BLI revealed that the signal intensities fluctuated dramatically in accord with the addition and withdrawal of progesterone (P_4) (Fig. 2c). In particular, tissue breakdown and regression after P_4-withdrawal and subsequent tissue regeneration faithfully reflected the decrease and increase in signal intensity, respectively (Fig. 2c). Thus, the repeated menstrual cycle-related changes of the transplants can be successfully reproduced and also noninvasively monitored in living NOG mice.

5.3 Discussion of This System

This animal model has several advantages over the current models of the endometrium and endometriosis.

First, the transplants are singly dispersed cells isolated from the human endometrium. A single-cell suspension is adequate for experimental procedures such as cell selection, genetic engineering, and quantitative assessment as compared to dissected sections. Quantification of the transplanted cells and the homogeneity of each model animal are especially and critically important for the comparative analysis of therapeutic agents. One potential disadvantage of singly dissociated cells is unpredicted scattering and spreading of the cells transplanted subcutaneously or intraperitoneally, making it difficult to identify the transplanted site and to evaluate the reconstructs. However, this limitation has been overcome by transplantation beneath the kidney capsule. Kidney capsule transplantation has the further advantage of being ideal for BLI assessment, not only of endometrial cells but other cell types as well, for example, (1) evaluation of cell type-dependent responses to tested drugs when two different types of cells are separately transplanted into each kidney, (2) easy macroscopic identification of the small reconstruct, and (3) efficient detection of the bioluminescent signals derived from the transplant because of the relatively superficial location on the kidney.

Second, the regenerated tissues in our model exhibit abundant vascularization, endometrial cell components, and tissue organization, all of which result in the long-term maintenance of the reconstructed structure and the hormone-dependent changes characteristic of human cycling endometrium and/or endometriotic explants. It is suitable for the evaluation of the effects of therapeutic reagents.

Third, the transplants can be assessed for a prolonged period in a noninvasive, real-time, and quantitative manner. Our lentiviral vector system [34] enables primary endometrial cells stably and permanently to express CBR luc, the light emitted from which has the capacity to pass through thicker tissues. Because of the advantages of the lentivirus and CBR luc, we were able to assess successfully the dynamic state of the endometrial reconstructs in living NOG mice.

By combining the unique potential of the human endometrium together with the special characteristics of NOG mice and lentivirus-mediated cell engineering, we are able to report on the first animal model suitable for the study of endometrial physiology/pathophysiology and the pathogenesis of endometriosis through non-invasive, real-time, and quantitative assessment of ectopically reconstituted endometrium-like tissues. Furthermore, this animal model system, based on the strategy of transplanting lentivirally engineered cells expressing a bioluminescent marker beneath the kidney capsule, can be potentially applicable for drug testing and gene target validation not only in endometriosis, but also in other various types of neoplastic disease.

Finally, BLI will provide novel methods to analyze biological processes, and it has a huge potential. In the near future, it will surely evolve and be developed to enable the visualization of two or three populations of cells simultaneously and to quantify cell numbers accurately depending on the innovative properties of detection systems and bioluminescent compounds. The visualization of many populations and improved quantification allow more complex kinetic analysis. Imaging studies using BLI in humans are limited, but information from the use of BLI in humanized mice will have a potentially great effect on clinical medicine. BLI will contribute to the modification and evaluation of preclinical trials, especially in the field of cell-based therapeutics, which will almost certainly demonstrate exponential expansion in the near future.

6 Conclusion

Recent animal models of human diseases (i.e., humanized mice) and in vivo imaging technologies are improving. These technologies will provide the opportunity for a new aspect in the field of animal experiments, delivering novel information and important insights.

Noninvasive and real time assessment with high sensitivity, accurate quantification, and high spatial resolution is ideal for imaging. In addition, the ideal modality requires obtaining images simply and in a short capture time.

Unfortunately, no modality and no animal model developed to date could fulfill all these requirements at once. However, the technology of each modality is improving every second. The combination of different imaging modalities (e.g., SPECT/CT, PET/CT, and FMT) is a novel powerful tool. Therefore, it is important to be familiar with in vivo imaging methods in humanized mice and to be able to choose suitable modalities as the occasion demands.

References

1. Balaban RS, Hampshire VA (2001) Challenges in small animal noninvasive imaging. ILAR J 42:248-62
2. Beekman FJ, van der Have F, Vastenhouw B, van der Linden AJ, van Rijk PP, Burbach JP, Smidt MP (2005) U-SPECT-I: a novel system for submillimeter-resolution tomography with radiolabeled molecules in mice. J Nucl Med 46:1194-200
3. Berger F, Lee YP, Loening AM, Chatziioannou A, Freedland SJ, Leahy R, Lieberman JR, Belldegrun AS, Sawyers CL, Gambhir SS (2002) Whole-body skeletal imaging in mice utilizing microPET: optimization of reproducibility and applications in animal models of bone disease. Eur J Nucl Med Mol Imaging 29:1225-36
4. Bremer C, Ntziachristos V, Weissleder R (2003) Optical-based molecular imaging: contrast agents and potential medical applications. Eur Radiol 13:231-43
5. Cao YA, Wagers AJ, Beilhack A, Dusich J, Bachmann MH, Negrin RS, Weissman IL, Contag CH (2004) Shifting foci of hematopoiesis during reconstitution from single stem cells. Proc Natl Acad Sci USA 101:221-6
6. Chatziioannou A, Tai YC, Doshi N, Cherry SR (2001) Detector development for microPET II: a 1 microl resolution PET scanner for small animal imaging. Phys Med Biol 46:2899-910
7. Chatziioannou AF (2002) Molecular imaging of small animals with dedicated PET tomographs. Eur J Nucl Med Mol Imaging 29:98-114
8. Cherry SR, Gambhir SS (2001) Use of positron emission tomography in animal research. ILAR J 42:219-32
9. Coatney RW (2001) Ultrasound imaging: principles and applications in rodent research. ILAR J 42:233-47
10. Contag CH, Contag PR, Mullins JI, Spilman SD, Stevenson DK, Benaron DA (1995) Photonic detection of bacterial pathogens in living hosts. Mol Microbiol 18:593-603
11. DeYoe EA, Bandettini P, Neitz J, Miller D, Winans P (1994) Functional magnetic resonance imaging (FMRI) of the human brain. J Neurosci Methods 54:171-87
12. Foster FS, Pavlin CJ, Harasiewicz KA, Christopher DA, Turnbull DH (2000) Advances in ultrasound biomicroscopy. Ultrasound Med Biol 26:1-27
13. Foster FS, Zhang MY, Zhou YQ, Liu G, Mehi J, Cherin E, Harasiewicz KA, Starkoski BG, Zan L, Knapik DA, Adamson SL (2002) A new ultrasound instrument for in vivo microimaging of mice. Ultrasound Med Biol 28:1165-72
14. Gao X, Cui Y, Levenson RM, Chung LW, Nie S (2004) In vivo cancer targeting and imaging with semiconductor quantum dots. Nat Biotechnol 22:969-76
15. Graves EE, Ripoll J, Weissleder R, Ntziachristos V (2003) A submillimeter resolution fluorescence molecular imaging system for small animal imaging. Med Phys 30:901-11
16. Green MV, Seidel J, Vaquero JJ, Jagoda E, Lee I, Eckelman WC (2001) High resolution PET, SPECT and projection imaging in small animals. Comput Med Imaging Graph 25:79-86
17. Griffin JL, Shockcor JP (2004) Metabolic profiles of cancer cells. Nat Rev Cancer 4:551-61
18. Hasegawa BH, Iwata K, Wong KH, Wu MC, Da Silva AJ, Tang HR, Barber WC, Hwang AH, Sakdinawat AE (2002) Dual-modality imaging of function and physiology. Acad Radiol 9:1305-21
19. Hastings JW (1996) Chemistries and colors of bioluminescent reactions: a review. Gene 173:5-11
20. Herschman HR (2003) Micro-PET imaging and small animal models of disease. Curr Opin Immunol 15:378-84
21. Honigman A, Zeira E, Ohana P, Abramovitz R, Tavor E, Bar I, Zilberman Y, Rabinovsky R, Gazit D, Joseph A, Panet A, Shai E, Palmon A, Laster M, Galun E (2001) Imaging transgene expression in live animals. Mol Ther 4:239-49

22. Ishizu K, Mukai T, Yonekura Y, Pagani M, Fujita T, Magata Y, Nishizawa S, Tamaki N, Shibasaki H, Konishi J (1995) Ultra-high resolution SPECT system using four pinhole collimators for small animal studies. J Nucl Med 36:2282-7
23. Ito M, Hiramatsu H, Kobayashi K, Suzue K, Kawahata M, Hioki K, Ueyama Y, Koyanagi Y, Sugamura K, Tsuji K, Heike T, Nakahata T (2002) NOD/SCID/γ_c^{null} mouse: an excellent recipient mouse model for engraftment of human cells. Blood 100:3175-82
24. Kaneko K, Yano M, Yamano T, Tsujinaka T, Miki H, Akiyama Y, Taniguchi M, Fujiwara Y, Doki Y, Inoue M, Shiozaki H, Kaneda Y, Monden M (2001) Detection of peritoneal micrometastases of gastric carcinoma with green fluorescent protein and carcinoembryonic antigen promoter. Cancer Res 61:5570-4
25. Koo V, Hamilton PW, Williamson K (2006) Non-invasive in vivo imaging in small animal research. Cell Oncol 28:127-39
26. Levenson RM, Mansfield JR (2006) Multispectral imaging in biology and medicine: slices of life. Cytometry A69:748-58
27. Levin CS (2005) Primer on molecular imaging technology. Eur J Nucl Med Mol Imaging 32 Suppl 2: S325-45
28. Liang HD, Blomley MJ (2003) The role of ultrasound in molecular imaging. Br J Radiol 76 Spec No 2: S140-50
29. Lin Y, Weissleder R, Tung CH (2002) Novel near-infrared cyanine fluorochromes: synthesis, properties, and bioconjugation. Bioconjug Chem 13:605-10
30. Mansfield JR, Gossage KW, Hoyt CC, Levenson RM (2005) Autofluorescence removal, multiplexing, and automated analysis methods for in-vivo fluorescence imaging. J Biomed Opt 10:41207
31. Massoud TF, Paulmurugan R, Gambhir SS (2004) Molecular imaging of homodimeric protein-protein interactions in living subjects. FASEB J 18:1105-7
32. Masuda H, Maruyama T, Hiratsu E, Yamane J, Iwanami A, Nagashima T, Ono M, Miyoshi H, Okano HJ, Ito M, Tamaoki N, Nomura T, Okano H, Matsuzaki Y, Yoshimura Y (2007) Noninvasive and real-time assessment of reconstructed functional human endometrium in NOD/SCID/gamma c^{null} immunodeficient mice. Proc Natl Acad Sci USA 104:1925-30
33. Michalet X, Pinaud FF, Bentolila LA, Tsay JM, Doose S, Li JJ, Sundaresan G, Wu AM, Gambhir SS, Weiss S (2005) Quantum dots for live cells, in vivo imaging, and diagnostics. Science 307:538-44
34. Miyoshi H, Blomer U, Takahashi M, Gage FH, Verma IM (1998) Development of a self-inactivating lentivirus vector. J Virol 72:8150-7
35. Nagai T, Ibata K, Park ES, Kubota M, Mikoshiba K, Miyawaki A (2002) A variant of yellow fluorescent protein with fast and efficient maturation for cell-biological applications. Nat Biotechnol 20:87-90
36. Nasir K, Budoff MJ, Post WS, Fishman EK, Mahesh M, Lima JA, Blumenthal RS (2003) Electron beam CT versus helical CT scans for assessing coronary calcification: current utility and future directions. Am Heart J 146:969-77
37. Natt O, Watanabe T, Boretius S, Radulovic J, Frahm J, Michaelis T (2002) High-resolution 3D MRI of mouse brain reveals small cerebral structures in vivo. J Neurosci Methods 120:203-9
38. Negrin RS, Contag CH (2006) In vivo imaging using bioluminescence: a tool for probing graft-versus-host disease. Nat Rev Immunol 6:484-90
39. Ntziachristos V, Tung CH, Bremer C, Weissleder R (2002) Fluorescence molecular tomography resolves protease activity in vivo. Nat Med 8:757-60
40. Ntziachristos V, Weissleder R (2002) Charge-coupled-device based scanner for tomography of fluorescent near-infrared probes in turbid media. Med Phys 29:803-9
41. Paulus MJ, Gleason SS, Easterly ME, Foltz CJ (2001) A review of high-resolution X-ray computed tomography and other imaging modalities for small animal research. Lab Anim (NY) 30:36-45
42. Phoon CK (2006) Imaging tools for the developmental biologist: ultrasound biomicroscopy of mouse embryonic development. Pediatr Res 60:14-21

43. Prout DL, Silverman RW, Chatziioannou A (2004) Detector concept for OPET-A combined PET and optical imaging system. IEEE Trans Nucl Sci 51:752-756
44. Rice BW, Cable MD, Nelson MB (2001) In vivo imaging of light-emitting probes. J Biomed Opt 6:432-40
45. Shah K, Jacobs A, Breakefield XO, Weissleder R (2004) Molecular imaging of gene therapy for cancer. Gene Ther 11:1175-87
46. Shaner NC, Steinbach PA, Tsien RY (2005) A guide to choosing fluorescent proteins. Nat Methods 2:905-9
47. Sweeney TJ, Mailander V, Tucker AA, Olomu AB, Zhang W, Cao Y, Negrin RS, Contag CH (1999) Visualizing the kinetics of tumor-cell clearance in living animals. Proc Natl Acad Sci USA 96:12044-9
48. Townsend DW (2001) A combined PET/CT scanner: the choices. J Nucl Med 42:533-4
49. Townsend DW, Cherry SR (2001) Combining anatomy and function: the path to true image fusion. Eur Radiol 11:1968-74
50. Troy T, Jekic-McMullen D, Sambucetti L, Rice B (2004) Quantitative comparison of the sensitivity of detection of fluorescent and bioluminescent reporters in animal models. Mol Imaging 3:9-23
51. Wakeling AE, Dukes M, Bowler J (1991) A potent specific pure antiestrogen with clinical potential. Cancer Res 51: 3867-73
52. Weissleder R (2001) A clearer vision for in vivo imaging. Nat Biotechnol 19:316-7
53. Weissleder R (2002) Scaling down imaging: molecular mapping of cancer in mice. Nat Rev Cancer 2:11-8
54. Wilson T, Hastings JW (1998) Bioluminescence. Annu Rev Cell Dev Biol 14:197-230
55. Zhao H, Doyle TC, Coquoz O, Kalish F, Rice BW, Contag CH (2005) Emission spectra of bioluminescent reporters and interaction with mammalian tissue determine the sensitivity of detection in vivo. J Biomed Opt 10:41210

Pseudoaneurysm of the uterine artery after laparoscopic myomectomy

Satoshi Asai, M.D., Hironori Asada, M.D., Masataka Furuya, M.D., Hitoshi Ishimoto, M.D., Mamoru Tanaka, M.D., and Yasunori Yoshimura, M.D.

Department of Obstetrics and Gynecology, Keio University School of Medicine, Tokyo, Japan

Objective: To describe a case of uterine pseudoaneurysm after laparoscopic myomectomy in a 36-year-old woman.
Design: Case report.
Setting: University hospital.
Patient(s): A 36-year-old woman, 3 months after laparoscopic myomectomy, presenting with an intrauterine hypoechoic lesion measuring 5 cm in diameter.
Intervention(s): Uterine pseudoaneurysm was diagnosed by color Doppler ultrasound.
Main Outcome Measure(s): Complete resolution of the pseudoaneurysm.
Result(s): Spontaneous thrombosis was observed in the pseudoaneurysm. At 6-month follow-up, the uterus appeared normal.
Conclusion(s): Our case presents the possibility of delayed occurrence of uterine pseudoaneurysm after laparoscopic myomectomy. (Fertil Steril 2008;■:■–■. 2008 by American Society for Reproductive Medicine.)

Key Words: Pseudoaneurysm, laparoscopic myomectomy, delayed occurrence

Pseudoaneurysm results from inadequate sealing of a laceration or puncture of the arterial wall during surgery or penetrating trauma. Uterine pseudoaneurysm is a rare complication of abortion, repeated curettage, pelvic surgery, cesarean section, or uncomplicated vaginal delivery (1–4). To date, there are four reported cases of postsurgical uterine artery pseudoaneurysms. The size of these pseudoaneursyms ranged from 2 to 3 cm (5). Color Doppler ultrasound is crucial for the diagnosis of pseudoaneurysm (1, 6, 7). Helvie et al. reported that this diagnostic modality showed a 94% sensitivity and 95% specificity in the detecting of pseudoaneurysms (8). The therapy options for uterine pseudoaneurysm include observation, hysterectomy, and uterine artery embolization.

The interval from pelvic surgery to the onset of symptoms has been reported to be between 1 week and 1 month (9–11). In this report, we describe a patient who developed pseudoaneurysm of the uterine artery 3 months after laparoscopic myomectomy.

CASE REPORT

A 36-year-old woman, gravida 0, para 1 was diagnosed as having an intramural myoma in the posterior wall that measured 5 cm in diameter. Her chief complaint was infertility. She underwent a laparoscopic myomectomy in our hospital. We used the four-puncture method under general anesthesia by endotracheal intubation in the lithotomy position. Vasopressin, 20 IU in 1 mL diluted 100 times with saline, was infused between the capsule of the myoma and normal muscle layer, and a horizontal incision was made just above the myoma using a harmonic scalpel. After the myoma was pulled and enucleated, a three-layer Z suture was used to close the myometrial layer employing 0 monofilament poliglecaprone 25 (Monocryl; Ethicon, Tokyo). All suturing procedures were performed intracorporeally. The enucleated myoma was removed with an electoromechanical morcellator (Sortz, Tuttlingen, Germany). Although a small hematoma (1 cm in diameter) was identified on day 3, the patient had an otherwise uneventful postoperative course and left the hospital on day 4.

Two months after surgery, transvaginal ultrasound showed a hypoechoic area measuring 2.4 cm in the corpus uterus. One month later, it reached 5 cm in diameter. Color Doppler ultrasound of the hypoechoic area demonstrated a turbulent arterial flow from the left uterine artery with a to-and-fro pattern, suggesting the presence of a pseudoaneurysm (Fig. 1A). At admission, the patient was asymptomatic, and her laboratory results, including white blood count, hemoglobin, hematocrit, fibrin split products, and fibrinogen, were normal. A magnetic resonance imaging (MRI) examination demonstrated a well-defined spherical mass (53 39 41 mm) in the anterior wall of the corpus uterus. The mass appeared inhomogeneously dark on T2W1 and slightly bright on T1W1 in the myometrium (Fig. 1B). An abdominal computed tomography scan performed 2 days after admission revealed partial thrombosis of the pseudoaneurysm. After

Received June 11, 2008; revised August 30, 2008; accepted September 4, 2008.
S.A. has nothing to disclose. H.A. has nothing to disclose. M.F. has nothing to disclose. H.I. has nothing to disclose. M.T. has nothing to disclose. Y.Y. has nothing to disclose.
Reprint requests: Satoshi Asai, M.D., Department of Obstetrics and Gynecology, Keio University School of Medicine, 35 Shinanomachi, Shinjuku-ku, Tokyo, Japan 160-8582 (FAX: 81-3-3226-1667; E-mail: tettyan@sc.itc.keio.ac.jp).

FIGURE 1

(A) Color Doppler ultrasound showed a swirling blood flow pattern within echogenic material in the uterine cavity (surrounded by arrows). This lesion was connected to the left uterine artery by a narrow neck (curved arrow). (B) Sagittal T2-weighted MRI of the pelvis. The signal void area (arrow) was from turbulent flow within the pseudoaneurysm. (C) Selective left uterine arteriogram. The arteriogram reflected a narrow neck to the pseudoaneurysm (arrows). (D) Follow-up transvaginal color Doppler ultrasound of the uterus. Complete resolution of the pseudoaneurysm was noted.

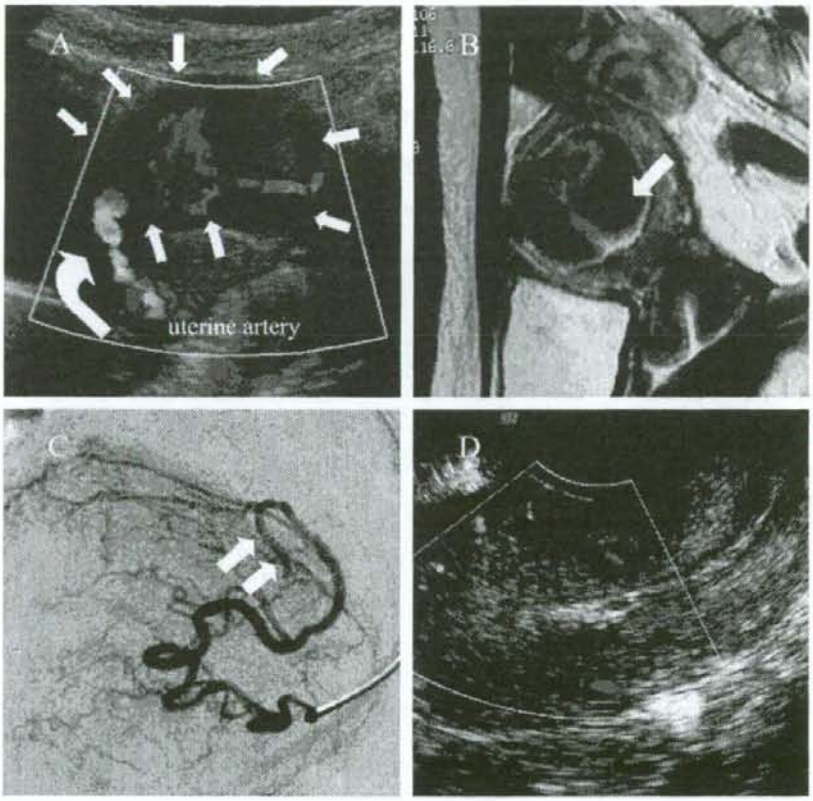

Asai. Uterine pseudoaneurysm after myomectomy. Fertil Steril 2008.

offering the patient an informed choice, conservative management with close monitoring was performed. Five days after admission, color Doppler ultrasound showed no flow in the pseudoaneurysm. Seven days after admission, she presented with sudden metrorrhagia. Laboratory tests showed anemia (hemoglobin, 9.5 g/dL) and a normal coagulation profile. The patient remained hemodynamically stable. The narrowness of the feeding artery hampered us from selectively catheterizing and embolizing the neck of the pseudoaneurysm (Fig. 1C). Fortunately, uterine bleeding spontaneously resolved.

Four months after surgery, centripetal thrombus formation was gradually increased in the pseudoaneurysm. At 6-month follow-up, the uterus appeared normal (Fig. 1D).

DISCUSSION

Pseudoaneurysm of the uterine artery is a rare cause of postoperative metrorrhagia. Pseudoaneurysm results from an arterial wall laceration or a puncture that allows blood to enter periarterial tissue and create a perfused sac that communicates with the parent artery lumen (12). The major difference from a true aneurysm is that the boundaries of a pseudoaneurysm are formed by a peripheral thrombus and are not surrounded by three arterial layers as in a true aneurysm (13). We performed color Doppler ultrasound for the diagnosis of uterine pseudoaneurysm in our case because color Doppler ultrasound is a useful diagnostic modality in the detection of blood flow and its direction in a cystic structure. Indeed, color Doppler ultrasound showed a high

sensitivity and specificity in the detection of uterine pseudoaneurysms (8).

Physical damage to the artery may lead to the development of pseudoaneurysm. Electrosurgery, usually used to achieve hemostasis during laparoscopic operations, could cause tissue damage (14). Indeed, electrosurgery causes significantly more tissue vessel damage than other techniques of hemostasis (15). For this reason, we adopted a more judicious use of bipolar electrosurgery, limiting the area of desiccation, to obtain hemostasis. Thus, the causal association between pseudoaneurysm and electrosurgery is not clear. To clarify this issue, we need further study.

The pseudoaneurysms of the uterus that have been reported so far occurred at earlier postoperative stages (9–11). However, while this manuscript was in preparation, Takeda et al. (5) reported a case in which a uterine pseudoaneurysm occurred as late as 2 months after laparoscopy-assisted myomectomy. In their case, the patient presented with sudden massive uterine hemorrhage that required emergent transarterial embolization. In our case, we also experienced a delayed occurrence of pseudoaneurysm; it took place 3 months after laparoscopic myomectomy. Our case was unique in that the whole spontaneous healing process of the uterine pseudoaneurysm with thrombosis formation was observed. Transarterial embolization has been accepted as the safest choice for uterine pseudoaneurysm. However, our experience suggests that urgent interventional therapy may not be necessary in all cases of uterine pseudoaneurysm. As more cases accumulate, a better understanding of its natural history will emerge, and more appropriate management will come to light.

REFERENCES

1. Zimon AE, Hwang JK, Principe DL, Bahado-Singh RO. Pseudoaneurysm of the uterine artery. Obstet Gynecol 1999;94:827–30.
2. Henrich W, Fuchs I, Luttkus A, Hauptmann S, Dudenhausen JW. Pseudoaneurysm of the uterine artery after cesarean delivery: sonographic diagnosis and treatment. J Ultrasound Med 2002;21:1431–4.
3. Kovo M, Behar DJ, Friedman V, Malinger G. Pelvic arterial pseudoaneurysm—a rare complication of cesarean section: diagnosis and novel treatment. Ultrasound Obstet Gynecol 2007;30:783–5.
4. McGonegle SJ, Dziedzic TS, Thomas J, Hertzberg BS. Pseudoaneurysm of the uterine artery after an uncomplicated spontaneous vaginal delivery. J Ultrasound Med 2006;25:1593–7.
5. Takeda A, Kato K, Mori M, Sakai K, Mitsui T, Nakamura H. Late massive uterine hemorrhage caused by ruptured uterine artery pseudoaneurysm after laparoscopic-assisted myomectomy. J Min Invas Gynecol 2008;15:212–6.
6. Hidar S, Bibi M, Atallah R, Essakly K, Bouzakoura C, Hidar M. [Pseudoaneurysm of the uterine artery: apropos of 1 case]. Journal de gynecologie, obstetrique et biologie de la reproduction 2000;29:621–4.
7. Wald DA. Postpartum hemorrhage resulting from uterine artery pseudoaneurysm. J Emerg Med 2003;25:57–60.
8. Helvie MA, Rubin JM, Silver TM, Kresowik TF. The distinction between femoral artery pseudoaneurysms and other causes of groin masses: value of duplex Doppler sonography. Am J Roentgenol 1988;150:1177–80.
9. Langer JE, Cope C. Ultrasonographic diagnosis of uterine artery pseudoaneurysm after hysterectomy. J Ultrasound Med 1999;18:711–4.
10. Lee WK, Roche CJ, Duddalwar VA, Buckley AR, Morris DC. Pseudoaneurysm of the uterine artery after abdominal hysterectomy: radiologic diagnosis and management. Am J Obstet Gynecol 2001;185:1269–72.
11. Higon MA, Domingo S, Bauset C, Martinez J, Pellicer A. Hemorrhage after myomectomy resulting from pseudoaneurysm of the uterine artery. Fertil Steril 2007;87:417e5–e8.
12. Kwon JH, Kim GS. Obstetric iatrogenic arterial injuries of the uterus: diagnosis with US and treatment with transcatheter arterial embolization. Radiographics 2002;22:35–46.
13. Descargues G, Douvrin F, Gravier A, Lemoine JP, Marpeau L, Clavier E. False aneurysm of the uterine pedicle: an uncommon cause of post-partum haemorrhage after caesarean section treated with selective arterial embolization. Eur J Obstet Gynecol Reprod Biol 2001;97:26–9.
14. Nezhat F, Seidman DS, Nezhat C, Nezhat CH. Laparoscopic myomectomy today. Why, when and for whom? Hum Reprod 1996;11:933–4.
15. Lantis JC, II, Durville FM, Connolly R, Schwaitzberg SD. Comparison of coagulation modalities in surgery. J Laparoendosc Adv Surg Techn 1998;8:381–94.

MHR-Basic Science of Reproductive Medicine Vol.14, No.1 pp. 17–22, 2008
Advance Access publication on January 4, 2008 doi:10.1093/molehr/gam081

Glycodelin blocks progression to S phase and inhibits cell growth: a possible progesterone-induced regulator for endometrial epithelial cell growth

Kuniaki Ohta[1,2], Tetsuo Maruyama[1,3], Hiroshi Uchida[1], Masanori Ono[1], Takashi Nagashima[1], Toru Arase[1], Takashi Kajitani[1], Hideyuki Oda[1], Mineto Morita[2] and Yasunori Yoshimura[1]

[1]*Department of Obstetrics and Gynecology, Keio University School of Medicine, 35 Shinanomachi, Shinjuku, Tokyo 160-8582, Japan;* [2]*Department of Obstetrics and Gynecology, Toho University School of Medicine, Tokyo 143-8541, Japan*

[3]Correspondence address. E-mail: tetsuo@sc.itc.keio.ac.jp

Prolonged exposure to unopposed estrogen in the absence of progesterone gives rise to endometrial hyperplasia and carcinoma. Post-ovulatory progesterone is necessary for the proper growth and differentiation of endometrial epithelial cells (EECs). Progesterone exposure induces the endometrial production of numerous bioactive substances, one of which is the glycoprotein, glycodelin (Gd). We investigated the role of Gd in cell cycle progression and cell growth to better understand how Gd affects EEC behavior and endometrial cancer pathogenesis. Ishikawa cells, a well-differentiated human endometrial epithelial cancer cell line, were transfected with expression plasmids encoding enhanced green fluorescent protein (EGFP) or EGFP-fused Gd (EGFP-Gd). They were then subjected to a cell proliferation assay, flow cytometry cell cycle analysis and RT–PCR analysis of cyclin-dependent kinase inhibitors (CDKIs) including p21, p27 and p16. Overexpression of EGFP-Gd resulted in a reduction of cell proliferation activity, an accumulation of G1-phase cells and up-regulation of p21, p27 and p16 mRNAs. Furthermore, progesterone-induced inhibition of Ishikawa cell growth was partially attenuated by Gd knockdown using siRNA. These results indicate that Gd causes inhibition of G1/S progression together with up-regulation of CDKIs thereby reducing cell growth. Thus, progesterone-induced expression of Gd may, at least in part, contribute to the suppression of endometrial epithelial growth observed during the secretory phase.

Keywords: glycodelin; endometrium; cell cycle; cyclin-dependent kinase inhibitors; progesterone

Introduction

Glycodelin (Gd) is a secretory phase dominant glycoprotein that is synthesized by endometrial epithelial cells (EECs) in response to progesterone exposure (Seppälä *et al.*, 2002). During the proliferative phase, the human endometrium contains no detectable Gd (Seppälä *et al.*, 1988; Waites *et al.*, 1988). However, it appears in some endometrial glands 4–5 days after ovulation, then gradually increases such that 10 days after ovulation all glands are strongly positive (Seppälä *et al.*, 2002). Its temporal and spatial expressions have made Gd a widely used marker of endometrial epithelial differentiation (Seppälä *et al.*, 2002). Gd inhibits oocyte–sperm binding in a dose-dependent manner (Oehninger *et al.*, 1995). Additionally, it has an immunosuppressive effect, potentially inactivating T cells and natural killer cells (Okamoto *et al.*, 1991). These observations suggest that Gd might contribute to contraceptive activity during the latter half of the secretory phase, and may also protect the embryonic semi-allograft from maternal immune insults. Aberrant expression of Gd has been reported in pathological conditions of the human endometrium and in endometrium-derived disorders including endometriosis (Seppälä *et al.*, 2002; Taylor *et al.*, 2002). Decreased immunostaining of Gd is associated with histologically retarded endometrium, suggesting that it protects against implantation failure (Klentzeris *et al.*, 1994). Malignant endometrium does not appear to synthesize Gd (Wood *et al.*, 1988), whereas serum Gd levels are elevated in patients with advanced endometriosis (Telimaa *et al.*, 1989).

We have previously reported that Gd is involved in histone deacetylase inhibitor-enhanced cytodifferentiation and cell motility in Ishikawa cells. These cells are a well-differentiated human EEC line (Uchida *et al.*, 2005, 2007). From these initial experiments, we noted that overexpression of Gd inhibited cell growth in Ishikawa cells. The objective of this study was to confirm this inhibitory effect of Gd on cell growth, elucidate its molecular basis and address the biological relevance of Gd in the behavior of EECs. We demonstrate here that Gd provokes G1 arrest with simultaneous up-regulation of genes that inhibit cell cycle progression and cell growth. In this manner, Gd behaves as an effector molecule for progesterone action.

Materials and methods

Reagents, plasmids and small interference RNA (siRNA)

Phenol red-free MEM and fetal bovine serum were purchased from Invitrogen Life Technologies (Tokyo, Japan). All oligonucleotides were synthesized by Invitrogen Life Technologies. Antibodies against Gd (Santa Cruz Biotechnology, Inc., Santa Cruz, CA, USA), green fluorescent protein (GFP)

(BD Biosciences, Bedford, MA, USA), mitogen-activated protein kinases (MAPK) (Upstate Biotechnology, Inc., Lake Placid, NY, USA) and horseradish peroxidase-conjugated secondary antibodies (Jackson ImmunoResearch Laboratories, West Grove, PA, USA) were purchased from commercial sources. Unless indicated otherwise, all other chemicals were obtained from Sigma-Aldrich Corp. (St. Louis, MO, USA) and Wako Biochemicals (Osaka, Japan). An expression plasmid harboring enhanced GFP (EGFP) or the EGFP-fused Gd gene (EGFP-Gd) and siRNAs for GAPDH and Gd were prepared as previously described (Uchida *et al.*, 2005, 2007).

Cell culture

The human EEC line Ishikawa (clone 3-H-12) was kindly provided by Dr Masato Nishida (National Kasumigaura Hospital, Ibaraki, Japan). The Ishikawa cells were maintained in phenol-red free MEM supplemented with 10% charcoal-treated fetal bovine serum, 100 U/ml penicillin and 100 mg/ml streptomycin at 37°C under 5% CO_2 in a humidified incubator and were used within 10 passages. For the proliferation assay, Ishikawa cells (2×10^5), transfected with expression plasmids encoding EGFP or EGFP-Gd using LipofectAMINE2000 (Invitrogen Life Technologies), Invitrogen Life Technologies were plated onto 12-well plates, cultured and harvested every 24 h by trypsinization and counted.

Cell proliferation assay (MTS assay)

Ishikawa cells were transfected with expression plasmids encoding EGFP or EGFP-Gd using LipofectAMINE2000 (Invitrogen Life Technologies), and sorted by flow cytometry based on the intensity of EGFP fluorescence 24 h later. The sorted cells (7×10^3 cells) were re-plated onto 96-well plates, grown for an additional 24 or 48 h and subjected to the Cell Titer 96 AQueous One Solution Cell Proliferation Assay (Promega Corp., Madison, WI, USA) using MTS (3-[4,5-dimethylthiazol-2-yl]-5-[3-carboxymethoxyphenyl]-2-[4-sulfophenyl]-2H-tetrazolium) according to the manufacturer's protocol. In brief, 20 µl of Cell Titer 96 AQueous One Solution Reagent was added into each well of the 96-well assay plate containing the samples in 100 µl of culture medium. The plate was incubated for 1.5 h at 37°C in a humidified, 5% CO_2 atmosphere. The absorbance at 490 nm was measured using the Ultrospec Visible Plate Reader II 96 (Amersham Biosciences, Piscataway, NJ, USA).

For knockdown experiments, Ishikawa cells were transfected without or with GAPDH or Gd siRNA, and treated without or with 1 µM progesterone in combination with 10 nM 17β-estradiol (EP) for 48 h, and then subjected to the MTS assay.

Cell cycle analysis by fluorescence-activated cell sorting and flow cytometry

The DNA distribution profiles of the EGFP- or EGFP-Gd-expressing cells were determined by a combination of cell sorting and flow cytometry using the EPICS ALTRA (Beckman coulter, Fullerton, CA, USA). Cultures transfected with expression plasmids encoding EGFP or EGFP-Gd were harvested, washed and resuspended at 1×10^7 cells/ml in media supplemented with 20 µg of Hoechst 33 342, a cell-permeable DNA dye and incubated for 45 min at 37°C. Cell suspensions were then filtered through a 5 ml Polystyrene Round-Bottom Tube with a Cell-Strainer Cap (BD Falcon, Bedford, MA, USA), and further incubated at room temperature with 5 µg/ml of propidium iodide (PI), a cell-impermeable DNA dye, for 5 min. The cells were sorted with the cytometer's Argon I-90 laser set at 488 nm in the primary position for EGFP and the Krypton laser 300 series tuned to a multiline ultraviolet spectrum in the secondary position for Hoechst 33 342. The EGFP signal was collected through a 450/50-band pass filter. The PI signal was excited with the Argon laser and collected through a 660/22-band pass filter. Both lasers were set with 100 mW of light. Each sample was sorted, and data were collected (10 000 events) using the EPICS ALTRA. Final analysis of the collected data, notably the DNA content histograms, was done using the software program MultiCycle (Beckman coulter). PI-positive cells and doublets were excluded to ensure that only single viable cells were subjected to the analysis of DNA content and EGFP expression.

RNA extraction and RT–PCR

Ishikawa cells were transfected with expression plasmids encoding EGFP or EGFP-Gd and cultured for 24 h before being harvested. EGFP-positive cells were then sorted by flow cytometry. Total RNA was extracted from the sorted cells using an RNA isolation kit (TAKARA, Tokyo, Japan). RT–PCR was carried out with 80 ng of total RNA using the One-Step RT–PCR kit (Qiagen, Hilden, Germany). The thermal cycling profile for p21, p27, p16 and GAPDH (glyceraldehyde-3-phosphate dehydrogenase (GAPDH)) was 50°C for 30 min as a hot start time step, 94°C for 15 min as an initial denaturation step, 25 cycles of 94°C for 1 min, 60°C for 1 min and 72°C for 1 min, followed by a final extension of 72°C for 10 min. Forward (F) and reverse (R) primers used in this study were as follows: p21, 5′-GTCCGTCAGAACCCATGC-3′ (F) and 5′-GGCGTTTGGAGTGGTAG AAA-3′ (R); p27, 5′-AAATGTTTCAGAC GGTTCCC-3′ (F) and 5′-ACAGGATGTCCATTCCATGA-3′ (R); p16, 5′-CACTCTCACCCGA CCCGT-3′ (F) and 5′-GCATGGTTACTGCCTCTG GT-3′ (R); and GAPDH, 5′-TCACCATCTTCCAGGAGCG-3′(F) and 5′-CTGCTTCACCACCTTCTT GA-3′(R). After PCR amplification, samples were electrophoresed in 2% agarose gels, followed by photographic recording of the ethidium bromide-stained gels with the FAS-III MINI (Toyobo, Tokyo, Japan). The band intensities were measured using Image J (version 1.38; http://rsb.info.nih.gov/ij/download.html). The relative ratio was calculated as the densitometry of each CDKI divided by that of GAPDH, and the relative ratio of EGFP-expressing cells was set at 1.0. All experimental data for RT–PCR represent the results obtained from three independent experiments.

Immunoprecipitation and immunoblotting

The procedures were described previously (Uchida *et al.*, 2005, 2007). In brief, Ishikawa cells transfected without or with siRNA were cultured for 3 days and lysed on ice with RIPA buffer (20 mM Tris–HCl, pH 7.5; 150 mM NaCl; 1 mM EDTA; 1% Na-deoxycholate; 0.1% sodium dodecyl sulfate; 1 mM Na3VO4; 50 mM NaF; 1 mM Na2MoO4) containing protease inhibitor cocktail (Roche, Basel, Switzerland). Protein concentrations were determined using DC protein assay kit (Bio-Rad Laboratories, Hercules, CA, USA) with BSA as a standard. Each 250 µg of protein was subjected to immunoprecipitation with anti-Gd antibody and protein G sepharose beads (Amersham Biosciences) for 3 h at 4°C. Immunoprecipitates were separated by electrophoresis on a 12% SDS–PAGE gel and transferred onto polyvinylidene difluoride membrane. After incubation with anti-Gd antibody, followed by horse-radish peroxidase-conjugated secondary antibody, the immunoreactive proteins were detected by the enhanced chemiluminescence method (Amersham Biosciences). Each input cell lysate (10 µg) was also subjected to immunoblotting with anti-MAPK antibody.

Statistical analysis

All statistical analyses were performed with the software package JMP version 6.0 (SAS Institute Inc., Cary, NC, USA). Data were analyzed by the Wilcoxon rank sum test, unpaired *t*-test or Dunnett's test following ANOVA. $P < 0.05$ was considered significant.

Results

Inhibition of cell growth by Gd

Gd expression is nearly undetectable in Ishikawa cells (Arnold *et al.*, 2002; Uchida *et al.*, 2005) and EECs of the proliferative phase (Seppälä *et al.*, 2002). Upon exposure to progestins and/or histone deacetylase inhibitors, however, Gd expression is induced in Ishikawa cells (Uchida *et al.*, 2005, 2007; Jaffe *et al.*, 2007) as well as in EECs of the secretory phase (Seppälä *et al.*, 2002). We began this study with experiments in which Gd was overexpressed in order to investigate its role in EEC function. We transfected Ishikawa cells with EGFP alone or EGFP-Gd to assess the effect of Gd on cell growth. The transfected cells (2×10^5 cells) were plated, cultured and harvested for counting cell number. Both types of transfected cells exhibited similar increases in number at 24 h after transfection; however, at 48 h, cells transfected

with EGFP-Gd had significant inhibition of cell growth when compared with cells transfected with EGFP alone (Fig. 1).

Although simple transfection with EGFP-Gd significantly inhibited cell growth, the reduction rate was only ~30% (Fig. 1). A larger reduction was not seen partly because of the relatively low (~20%) transfection efficiency of EGFP-Gd. To minimize the influence of untransfected cells, EGFP-positive Ishikawa cells were sorted by flow cytometry 24 h after transfection of EGFP or EGFP-Gd, based on the intensity of EGFP fluorescence (Fig. 2A). The cells obtained from sorting following transfection of the different plasmids were designated as EGFP- or EGFP-Gd-expressing cells. They were then plated, cultured and harvested 48 and 72 h after transfection, and subjected to the MTS assay. The EGFP-Gd-expressing cells exhibited a significant reduction (50%) in proliferation activity (Fig. 2B).

Inhibition of G1 to S cell cycle progression by Gd

To examine whether the retardation of cell growth was due to the inhibition of cell cycle progression, we analyzed the cell cycle distribution of purified Ishikawa cells overexpressing EGFP or EGFP-Gd. Flow cytometric analysis revealed that EGFP-Gd-expressing cells accumulated in the G1 phase of the cell cycle, with a concomitant decrease in the proportion of those in the S and G2/M phases, as compared to EGFP-expressing cells (Figs. 3A and B). These changes in cell cycle distribution were observed at 24 h after transfection and became more evident and statistically significant at 48 h (Fig. 3B).

To determine whether the inhibitory effect of Gd on cell growth was dose-dependent, we compared the cell cycle distribution between transfected Ishikawa cells with high and low levels of Gd expression. As shown in Fig. 3C, EGFP-positive cells were further gated based on the intensity of EGFP fluorescence and were divided into two distinct populations: high and low. Cell cycle analysis of each gated population revealed that high EGFP-Gd-expressing cells significantly accumulated in the G1 phase with a concomitant decrease in the proportion in S phase (Fig. 3D). The patterns of cell cycle distribution were similar among the other three populations (Fig. 3D).

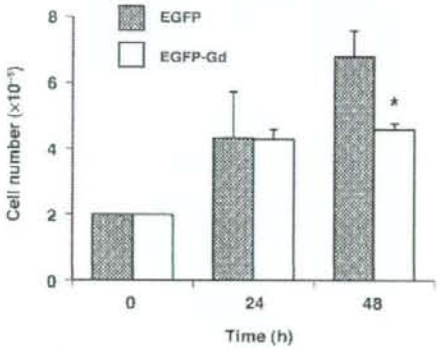

Figure 1: Inhibition of cell growth by transfection with EGFP-Gd
Ishikawa cells (2×10^5 cells) transfected with EGFP or EGFP-Gd were plated onto 12-well plates, cultured and harvested for cell counting over the indicated time course. *$P < 0.05$ versus EGFP (ANOVA and unpaired *t*-test)

Up-regulation of cyclin-dependent kinase inhibitors by Gd

Cyclin-dependent kinase (CDK) inhibitors including p21, p27 and p16 are well-known negative regulators of the G1/S transition (Shapiro, 2006). Overexpression and/or induction of these CDK inhibitors (CDKIs) lead to G0/G1 accumulation (Shapiro, 2006). To address a possible involvement of CDKIs in the inhibition of the G1/S transition by Gd, we examined the expression of p21, p27 and p16 in EGFP- or EGFP-Gd-expressing cells by RT–PCR. EGFP-Gd significantly up-regulated the levels of p21, p27 and p16 mRNAs 48 h after transfection (Fig. 4). GAPDH, an internal control gene, was constant among each group of transfected and sorted cells (Fig. 4).

Attenuation of progesterone-induced inhibition of Ishikawa cell growth by Gd knockdown using siRNA

Progesterone inhibits cell growth in Ishikawa cells while simultaneously up-regulating Gd (Uchida *et al.*, 2005, 2007). This raises the possibility that progesterone-induced Gd may be involved in the inhibition of EEC cell growth. To test this, Ishikawa cells were transfected without or with siRNA for GAPDH or Gd, and treated without or with EP for 48 h, prior to being used in the MTS assay.

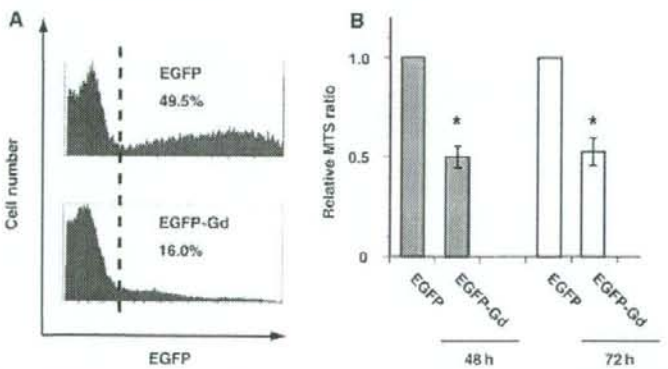

Figure 2: Inhibition of cell growth by overexpression of EGFP-Gd
(**A**) Flow cytometry analysis of Ishikawa cells transfected with EGFP or EGFP-Gd. The transfected cells were cultured for 24 h, harvested and subjected to flow cytometric analysis of EGFP fluorescence and DNA content. The broken line separates EGFP-positive cells from negative cells. The percentages of the corresponding EGFP-positive cells are described in each panel. (**B**) MTS assay of the sorted Ishikawa cells following transfection. EGFP-positive cells as indicated in (A) were sorted by flow cytometry 24 h after transfection, plated onto 96-well plates, cultured for another 24 h (gray bars) or 48 h (white bars) and then subjected to the MTS assay. Bars indicate the means ± SD of the relative MTS ratio obtained from six independent experiments. The MTS value of EGFP-expressing cells was set at 1.0. *$P < 0.01$ versus EGFP (Wilcoxon rank sum test)

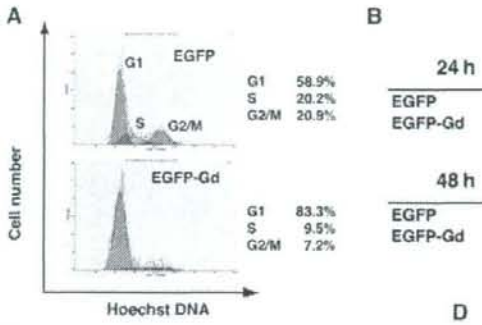

B

24 h	Percent of cells in phase		
	G1	S	G2/M
EGFP	52.3 ± 7.2	24.0 ± 3.9	22.6 ± 4.3
EGFP-Gd	59.0 ± 10.6	20.0 ± 4.9	21.1 ± 6.1

48 h	Percent of cells in phase		
	G1	S	G2/M
EGFP	55.1 ± 3.8	23.4 ± 2.0	21.6 ± 2.1
EGFP-Gd	65.9* ± 8.8	18.0* ± 4.3	15.8* ± 5.0

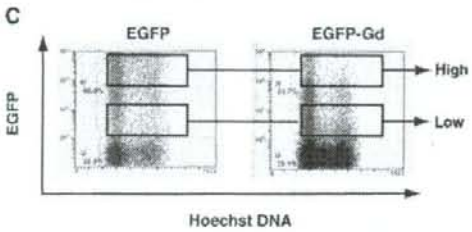

D

EGFP	Percent of cells in phase		
	G1	S	G2/M
High	52.0 ± 3.1	23.8 ± 0.4	23.8 ± 3.8
Low	54.0 ± 2.7	24.7 ± 2.4	21.4 ± 2.1

EGFP-Gd	Percent of cells in phase		
	G1	S	G2/M
High	71.7* ± 5.8	14.6* ± 3.5	17.5 ± 7.6
Low	56.3 ± 3.3	21.8 ± 1.0	20.9 ± 3.4

Figure 3: Inhibition of G1/S transition by overexpression of EGFP-Gd
(**A**) Flow cytometric analysis of Ishikawa cells transfected as indicated. Ishikawa cells were transfected with EGFP or EGFP-Gd and cultured for 48 h. EGFP-positive cells were sorted and subjected to FACS analysis of DNA content. (**B**) Cell cycle distribution of Ishikawa cells transfected as indicated. Cell cycle distribution was analyzed using Multicycle software. The values represent the means ± SD from six independent experiments. $^*P < 0.05$ versus EGFP (ANOVA and unpaired *t*-test). (**C**) Flow cytometric analysis of Ishikawa cells expressing high or low levels of Gd. Ishikawa cells were transfected with EGFP or EGFP-Gd and cultured for 48 h. The cells were harvested and subjected to FACS analysis of EGFP fluorescence and DNA content. Cell populations with high and low levels of EGFP and EGFP-Gd expression were determined as indicated. (**D**) Cell cycle distribution of Ishikawa cells expressing high or low levels of Gd. Cell cycle distribution of the gated populations as indicated in (C) was analyzed using Multicycle software. The values represent the means ± SD from five independent experiments. $^*P < 0.05$ versus EGFP (ANOVA and unpaired *t*-test)

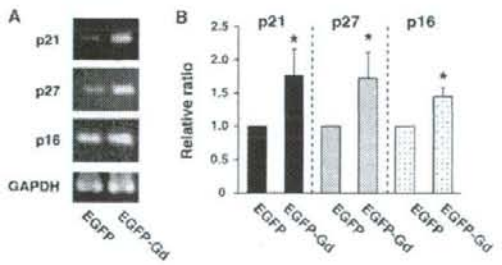

Figure 4: Induction of CDKIs by overexpression of EGFP-Gd
(**A**) Representative agarose gel images of RT-PCR products as indicated. Ishikawa cells were transfected as indicated, cultured for 48 h, sorted by flow cytometry based on the intensity of EGFP fluorescence and then harvested for extraction of total RNA. The expression levels of p21, p27, p16 and GAPDH mRNAs were analyzed by RT-PCR and densitometry. (**B**) Bars indicate the mean ± SD of the relative mRNA expression of the CDKIs from three independent experiments. $^*P < 0.05$ versus EGFP (Wilcoxon rank sum test)

In agreement with previous studies (Uchida *et al.*, 2005, 2007), treatment with EP-induced Gd expression, and the induction of Gd by EP treatment, is largely repressed by Gd siRNA, but not GAPDH siRNA (Fig. 5A). Furthermore, we showed that treatment with EP significantly inhibited cell growth (Fig. 5B). Importantly, the inhibitory effect was significantly abrogated by Gd siRNA, but not by GAPDH siRNA (Fig. 5B).

Discussion

CDK is a protein kinase involved in regulating the cell cycle. It is activated by associating with a cyclin, forming a CDK complex. CDKIs, including p21, p27 and p16, are a group of proteins that interact with and inhibit the CDK complex. This negatively affects cell cycle progression thereby retarding cell growth (Shapiro, 2006). In the present study, overexpression of Gd alone inhibited the G1/S transition and cell growth, and also increased expression of p21, p27 and p16. Thus, Gd-induced G1 arrest may be, at least in part, attributable to the up-regulation of CDKIs by Gd.

Gd appears in some endometrial glands 4–5 days after ovulation, then gradually increases such that at 10 days after ovulation all glands are strongly positive (Seppälä *et al.*, 2002). The induction of endometrial Gd is dominantly regulated by progesterone (Seppälä *et al.*, 2002). Ishikawa is a well-differentiated endometrial cancer cell line of human glandular epithelial origin that expresses functioning estrogen receptor α and the progesterone receptor (PR). These qualities have led to its widespread use for studies of human EEC pathophysiology (Nishida, 2002). Indeed, Ishikawa cells possess similar properties to normal EECs (Nishida, 2002), including the ability to express Gd in response to progesterone (Uchida *et al.*, 2005). A close association between progesterone-induced Gd expression and cell growth inhibition was evident in our study. This suggests a possible mechanism by which progesterone-induced Gd may inhibit cell growth of EECs during the late secretory phase. In agreement, several studies have reported that Ki-67, a cell proliferation marker, is down-regulated, whereas p21 and p27 are

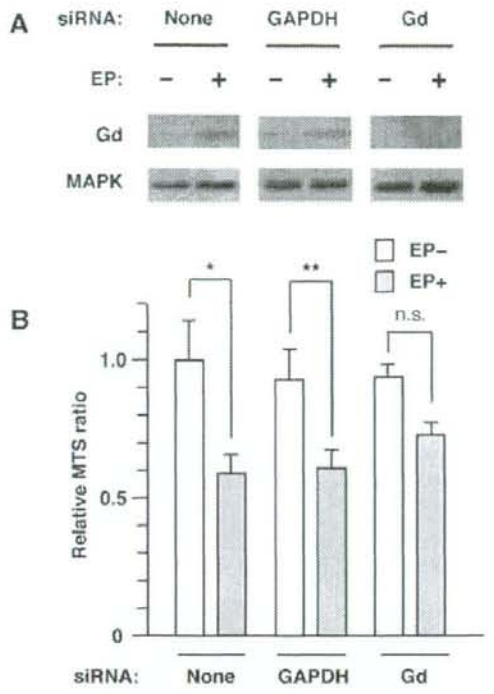

Figure 5: Attenuation of progesterone-induced inhibition of Ishikawa cell growth by Gd siRNA
(**A**) Ishikawa cells were untransfected (none) or transfected with GAPDH siRNA or Gd siRNA, treated without or with EP for 3 days and harvested. Total cell lysates were extracted and subjected to immunoprecipitation and immunoblotting with anti-Gd antibody (upper panels). Each input cell lysate was subjected to immunoblotting with anti-MAPK antibody (lower panels). (**B**) Ishikawa cells were untransfected (none) or transfected with GAPDH siRNA or Gd siRNA, treated without (EP-, white bar) or with EP (EP+, gray bar) for 48 h and then subjected to the MTS assay. Bars indicate the mean ± SD of the relative MTS ratio obtained from four independent experiments. MTS value of EP-untreated cells without siRNA transfection was set at 1.0. $*P < 0.01$; $**P < 0.05$; n.s., not significant (ANOVA and Dunnett's test)

up-regulated in EECs during the secretory phase (Shiozawa *et al.*, 1998; Toki *et al.*, 1998; Bebington *et al.*, 2000). Notably, although Gd siRNA abrogated progesterone-induced Gd expression (Uchida *et al.*, 2005, 2007), it only partially rescued the inhibition of Ishikawa cell growth. This suggests that progesterone-regulated gene product(s) other than Gd may also contribute to the inhibitory effects. Given the up-regulation of CDKIs by Gd overexpression, Gd may be, at least in part, involved in the inhibition of cell growth together with up-regulation of CDKIs in EECs during the secretory phase.

The PR activates the natural promoters for p21, p27, p16 and Gd (Tung *et al.*, 1993; Owen *et al.*, 1998; Gao *et al.*, 2001; Smid-Koopman *et al.*, 2003; Gizard *et al.*, 2005). In particular, p21, p27 and Gd promoters are stimulated by the PR through G/C-rich (Sp1 binding) elements, but not through the functional classical response element (Tung *et al.*, 1993; Owen *et al.*, 1998; Gao *et al.*, 2001; Gizard *et al.*, 2005). Although it is unknown whether Sp1 is involved in PR-induced up-regulation of p16, Sp1 is required for the activation of the p16 promoter in human fibroblasts (Wu *et al.*, 2007). We demonstrated that overexpression of Gd alone resulted in the induction of p21, p27 and p16 in the absence of progesterone. These findings raise the possibility that the PR induces Gd, which, in turn, may augment the induction of the CDKIs, by PR, through Sp1 sites. In this regard, PR-induced Gd may act inside the cell, since Ishikawa cells are not capable of secreting Gd (Arnold *et al.*, 2002). Although the function of intracellular Gd is poorly understood, it has been reported to mediate the histone deacetylase inhibitor-driven induction of leukemia inhibitory factor (Uchida *et al.*, 2005). Additionally, it also regulates the expression of several genes including MUC1, vimentin, E-cadherin and cytokeratins 8 and 18 (Kämäräinen *et al.*, 1997; Koistinen *et al.*, 2005).

Gd has been observed in various benign and malignant tumors (Seppälä *et al.*, 2002). Intriguingly, Gd expression in cancer is positively associated with a good prognosis (Mandelin *et al.*, 2003; Shabani *et al.*, 2005). Chemotherapy-treated patients with Gd-expressing serous ovarian carcinoma have longer survival times than those with Gd-negative tumors with the same differentiation grade and clinical stage (Mandelin *et al.*, 2003). Furthermore, patients with Gd-positive breast tumors have a better prognosis when compared with patients with Gd-negative tumors (Mandelin *et al.*, 2003; Shabani *et al.*, 2005). The improved prognosis may be the result of a combination of Gd actions including induction of cytodifferentiation (Kämäräinen *et al.*, 1997; Uchida *et al.*, 2005) and apoptosis (Koistinen *et al.*, 2005), as well as its anti-proliferative activity (Kämäräinen *et al.*, 1997; Koistinen *et al.*, 2005). In this regard, Gd may be useful not only as a marker but also as a targeting molecule in the management and treatment of endometrial cancer and other endometrium-derived diseases.

In summary, Gd causes inhibition of G1/S progression together with up-regulation of CDKIs, thereby reducing cell growth. Gd may be, at least in part, responsible for the progesterone-mediated inhibition of cell growth. Thus, progesterone-induced expression of Gd during the secretory phase may contribute to the suppression of endometrial epithelial growth. Gd may act as an inducible effector molecule of progesterone action, possibly regulating the growth and differentiation of EEC's during the menstrual cycle. In controlling endometrial growth, it may prevent the progression of endometrium-derived diseases including endometrial cancer.

Acknowledgements

We thank Dr Masato Nishida (National Kasumigaura Hospital, Ibaragi, Japan) for Ishikawa cells; members of the T.M. laboratory for technical assistance and helpful advice; and Rika Shibata for secretarial assistance.

Funding

Grant-in-Aids from the Japan Society for the Promotion of Science (JSPS) (to T.M., K.O., H.U. and Y.Y.) and by grants from the Keio Health Counseling Center (to T.M.).

References

Arnold JT, Lessey BA, Seppälä M, Kaufman DG. Effect of normal endometrial stroma on growth and differentiation in Ishikawa endometrial adenocarcinoma cells. *Cancer Res* 2002;**62**:79–88.

Bebington C, Doherty FJ, Ndukwe G, Fleming SD. The progesterone receptor and ubiquitin are differentially regulated within the endometrial glands of the natural and stimulated cycle. *Mol Hum Reprod* 2000;**6**:264–268.

Gao J, Mazella J, Seppälä M, Tseng L. Ligand activated hPR modulates the glycodelin promoter activity through the Sp1 sites in human endometrial adenocarcinoma cells. *Mol Cell Endocrinol* 2001;**176**:97–102.

Gizard F, Robillard R, Gervois P, Faucompre A, Revillion F, Peyrat JP, Hum WD, Staels B. Progesterone inhibits human breast cancer cell growth through transcriptional upregulation of the cyclin-dependent kinase inhibitor p27Kip1 gene. *FEBS Lett* 2005;**579**:5535–5541.